Biomimetic Synthesis of Ear-of-wheat-shaped Manganese Oxide Nanoparticles on Carbon Nanotubes for High-capacity Lithium Storage

Xiaofei Sun, Meijuan Li, Anastase Ndahimana, Peng Ding, Youlong Xu*, Qiongdan Hu, Kai Chen* [iD], and Tianyu Feng

Manganese oxide (Mn_3O_4) is of great potential for lithium storage based on conversion reactions, but its application in rechargeable lithium batteries is severely hindered by the low electric conductivity and large volume variation during lithiation/delithiation. Herein, a biomimetic ear-of-wheat-like nanocomposite of ultrafine Mn_3O_4 nanoparticles (MONPs) and multi-walled carbon nanotubes (MWCNTs) is prepared using a facile solvothermal method. The tightly packed MONP "cereal-grains" are directly grown and uniformly interspersed on the outer surface of skeleton MWCNT "central stems." The ultrafine MONPs are favorable to lithium incorporation/extraction while the interconnected MWCNT skeletons provide a highly conducting network for electron transportation. Consequently, a high reversible capacity of 810 mA h g^{-1} is obtained at the current density of 40 mA g^{-1}. After 50 cycles at 160 mA g^{-1}, the nanocomposite still delivers a capacity up to 796 mA h g^{-1}, which is higher than twice of that of pure Mn_3O_4 nanopowders. The unique nanostructure and the facile biomimetic method can be widely extended to design and explore various high-performance energy materials for lithium/sodium ion batteries and fuel cells.

1. Introduction

Lithium-ion batteries (LIBs) are being increasingly used in portable electronic devices, electric vehicles and smart grid energy storage applications.[1,2] Electrode active materials that are capable of reversible lithium storage play a crucial role on the electrochemical performance of LIBs.[3–5] Graphite has been vastly used as the main anode material since the commercialization of LIBs in 1990s, due to its superior cycling performance and low-cost advantage.[6] However, the theoretical specific capacity of graphite is only 372 mA h g^{-1}, and safety issues might be caused once it is over charged/discharged at higher rates. Hence, graphite cannot meet the ever-growing energy storage demand in the matter of energy density and safety concerns,[7–9] and great efforts have been devoted to explore new anode materials for higher capacities and better safety performance.[10–12]

Poizot et al. proposed that lithium could be stored reversibly in transition metal oxides (M_xO_y, M = Fe, Co, Ni, Cu, etc.) through heterogeneous conversion reactions according to $M_xO_y + 2yLi^+ + 2ye^- \leftrightarrow xM^0 + yLi_2O$.[13,14] As one of the promising transition metal oxide anodes for LIBs, Mn_3O_4 shows a theoretical capacity as high as ~937 mA h g^{-1} in addition to natural abundance and environmental friendliness. However, the low electric conductivity ($\sim 10^{-7}$–10^{-8} S cm^{-1}) and high volume expansion/contraction during charging/discharging limit its capacity, cycling, and rate performances greatly.[15–17] Particle down-sizing, exotic elemental doping, and especially nanostructure designing are widely employed to overcome these drawbacks.[7,18–21] For example, Ma et al. reported Fe-doped Mn_3O_4 with a hierarchical porosity connected by macropores and mesopores,[22] Zhang et al. used Zn_2SnO_4 nanoneedles to prepare one-dimensional Mn_3O_4/Zn_2SnO_4 hybrid composites,[23] and Zhang et al. synthesized ternary $MnCO_3/Mn_3O_4/RGO$ composites utilizing reduced graphene oxide (RGO).[24] The electrochemical performance of Mn_3O_4 is partially improved but still far away from practical application. Moreover, the synthesis methods for these nanomaterials are generally complicated and time-cosuming, thus are not conducive to industrial production.

Herein, we report a facile and fast solvothermal synthesis of the ear-of-wheat-shaped nanocomposite of ultrafine Mn_3O_4 nanoparticles

Prof. X. Sun
Electronic Materials Research Laboratory, Key Laboratory of the Ministry of Education & International Center for Dielectric Research, Xi'an Jiaotong University, Xi'an Shaanxi 710049, China

State Key Laboratory for Manufacturing Systems Engineering, School of Mechanical Engineering, Xi'an Jiaotong University, Xi'an Shaanxi 710049, China
M. Li, Dr. A. Ndahimana
State Key Laboratory for Manufacturing Systems Engineering, School of Mechanical Engineering, Xi'an Jiaotong University, Xi'an Shaanxi 710049, China
P. Ding, Prof. Y. Xu, Q. Hu, Dr. T. Feng
Electronic Materials Research Laboratory, Key Laboratory of the Ministry of Education & International Center for Dielectric Research, Xi'an Jiaotong University, Xi'an Shaanxi 710049, China
E-mail: ylxu@xjtu.edu.cn
Prof. K. Chen
State Key Laboratory for Mechanical Behavior of Materials, Center for Advancing Materials Performance from the Nanoscale (CAMP-Nano), Xi'an Jiaotong University, Xi'an Shaanxi 710049, China
E-mail: kchenlbl@gmail.com
[iD] The ORCID identification number(s) for the author(s) of this article can be found under https://doi.org/10.1002/eem2.12069.

(MONPs) with multi-walled carbon nanotubes (MWCNTs). Electro-chemical characterization demonstrates that the biomimetic MWCNTs/MONPs nanocomposite exhibits superb capacity, rate, and cycling performances as a novel anode material for LIBs. The morphology and crystallographic structure are studied in detail, and the mechanism of the excellent performance is discussed as well.

2. Results and Discussion

The MWCNTs/MONPs nanocomposite was prepared following a facile solvothermal method as illustrated in Scheme 7. The as-received MWCNTs were first functionalized to remove impurities of carbon ash and residual catalysts, and to code functional groups such as –OH and –COOH on the surface of MWCNTs.[25,26] As can be seen from the scanning electron microscope (SEM) image in **Figure 1**a, the tangled as-received nanotubes are separated into individual smooth ones with better solubility after functionalization.[27] The outer diameter of the functionalized MWCNTs ranges predominantly from 15 to 19 nm. MONPs were then directly grown on MWCNTs via a simple one-pot solvothermal route. The MONPs are tightly grown on the surface of MWCNTs forming a biomimetic ear-of-wheat-like composite. The MONP "cereal-grains" is uniformly interspersed on the skeleton MWCNT "central stems" as shown in **Figure 1**b. The outer diameter of the MWCNTs/MONPs nanocomposite is thus increased to 38–48 nm. At the meantime, the diameter of MONPs is found spans from 10 nm to 30 nm. Besides carbon element, EDX spectrum in the inset of **Figure 1**b also successfully detects Mn and O. One needs to note that the Al peak comes from the sample holder while Pt is introduced during sample preparation. The actual mass ratio of Mn_3O_4 in the MWCNTs/MONPs nanocomposite is roughly 69% according to elemental analysis. As observed in **Figure 1**c, two independent MWCNTs are fully coated by Mn_3O_4, revealing the biomimetic ear-of-wheat-shaped nanostructure of the MWNCTs/MONPs composite. In comparison, a bare MWCNT that is not coated by anything with a diameter of 17 nm is happen to be found in the same picture. **Figure 1**d shows the XRD pattern of the obtained MWCNTs/MONPs nanocomposite using Cu Kα radiation. The crystal structure can be indexed as the tetragonal haus-mannite phase of Mn_3O_4 (JCPDS No. 24-0734) with the space group of $I4_1/amd$ (space group No. 141). All the diffraction peaks are well assigned to Mn_3O_4 except the weak peak at 26.3° that corresponds to

hexagonal carbon in MWCNTs (JCPDS No. 01-075-1621), and no other phases are observed. Based on the tetragonal Mn_3O_4 model,[28] Rietveld refinement on the XRD pattern demonstrates the good crystallinity of the sample material. The agreement of the fitness is as follows: $R_p = 2.30\%$, $R_{wp} = 2.90\%$, and $R_{Bragg} = 0.37\%$. The lattice parameters are calculated as: $a = b = 5.7625(2)$ Å, $c = 9.4524(9)$ Å, $\alpha = \beta = \gamma = 90°$, $V = 313.8855(0)$ Å^3, and $V/Z = 78.4713(8)$ Å^3, which all agree well with the reported values.

The microstructure of the MWCNTs/MONPs nanocomposite is further verified by transmission electron microscope (TEM). The TEM image in **Figure 2**2a shows that MONPs tightly pack on the surface of MWCNTs in good consistence with the biomimetic ear-of-wheat-like morphology shown in **Figure 1**b,c. The stick diameter and particle size also agree well with the SEM results. The crystal lattice fringes can be clearly observed by high resolution TEM (HRTEM) image in **Figure 2**b. The profiling interpretation is also shown in **Figure 2**c. The interference fringe spacing is about 0.278 nm, corresponding exactly to the interplanar distance of the (013) plane of Mn_3O_4. Therefore, in combination of the XRD, EDX, SEM, and TEM analysis, homogenous ear-of-wheat-like MWCNTs/MONPs nanocomposite with good crystallinity is readily prepared by our solvothermal synthesis.

The electrochemical performance of the MWCNTs/MONPs nanocomposite is evaluated using CR2016 coin cells. The typical voltage profiles of the initial five discharge/charge cycles between 0.01 V (vs Li/Li$^+$, hereafter) and 3.0 V are shown in **Figure 3**a. The discharge curve of the first cycle could be distinctly divided into three segments. The sloping voltage from ~1.65 V to ~0.28 V is ascribed to the formation of solid-electrolyte interphase (SEI) and the incipient reduction of Mn_3O_4. The well-defined voltage plateau at around 0.25 V is attributed to the lithium storage reaction according to: $Mn_3O_4 + 8Li^+ + 8e^- \rightarrow 3Mn~(0) + 4Li_2O$.[29] The tailing slope thereafter results from the possible decomposition of electrolytes at low voltages and further lithium storage via interfacial charging.[30] Due to such side reactions, the initial specific discharge capacity reaches ~1 528 mA h g^{-1}, tremendously exceeding the theoretical capacity of lithium storage in Mn_3O_4 based solely on a conversion reaction. The discharge voltage plateau shifts to around 0.40 V from the second cycle, slightly higher than that of the first cycle, indicating the Li$^+$ incorporation reaction has become easier.[31] The average charging voltage is about 1.25 V, which is 0.9, 0.8, 0.7, and 0.4 V lower than that of Co_3O_4,[32] CuO,[33] NiO,[34] and Fe_3O_4,[35] respectively. It is
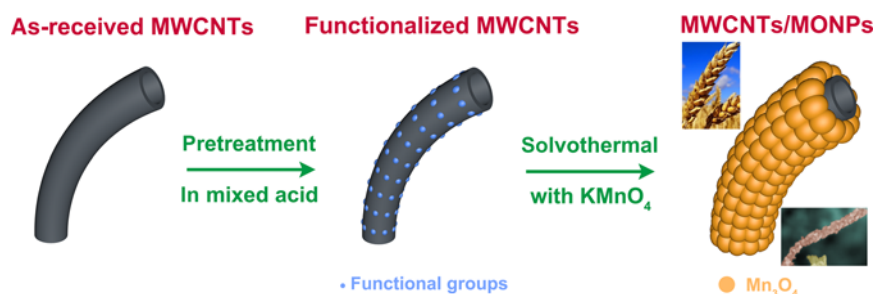
Scheme 1. Schematic illustration of the biomimetic synthesis of the ear-of-wheat-shaped MWCNTs/MONPs nanocomposite.
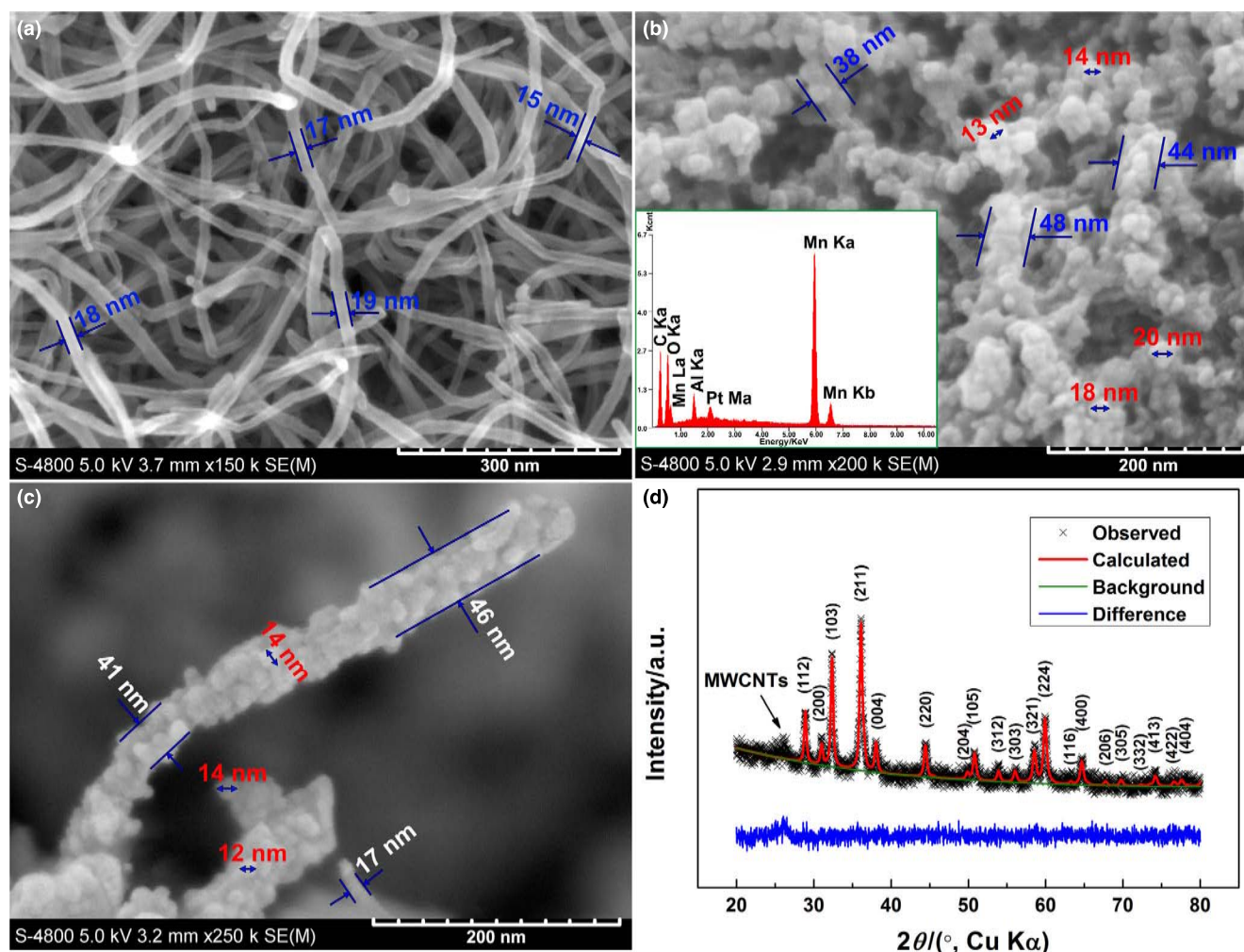
Figure 1. SEM images of the functionalized MWCNTs a) and the biomimetic MWCNTs/MONPs nanocomposite b,c) as well as the X-ray diffraction pattern of MWCNTs/MONPs d). The inset of b) shows the corresponding EDX spectrum. The goodness of Rietveld refinement in d) is as follows: R_p = 2.30%, R_{wp} = 2.90%, R_{Bragg} = 0.37%.

therefore favorable to increasing the operation voltage as well as energy density of the full battery when practically coupled with appropriate cathodes. An additional charging shoulder is observed at higher voltages (above 2 V) due to the oxidation of MnO to Mn_3O_4.[36] The reversible charge capacity of the first cycle is ~810 mA h g^{-1}, comparable to reported leading capacity of Mn_3O_4 anode materials, and is much higher than the theoretical capacity of commercial graphitic carbon (~372 mA h g^{-1}).[16] The discharge/charge profiles follow similar configurations from the second cycle except for little capacity decay upon cycling. The cyclic voltammetry (CV) curves in the inset of **Figure 3**a essentially agree well with the discharge/charge profiles, except that the ~0.25 V platform and the subsequent slope in the first discharge profile are promiscuously shown in the cyclic voltammogram as a long sharp peak, which may correlate with the initial synergy of the electrode during CV-sweep. It is worth noting that the discharge/charge profiles and CV curves become stable and nearly overlapping from the second cycle, indicating the high electrochemical reversibility and structural stability of the MWCNTs/MONPs composite electrode in the subsequent cycles.

The long-term cycling stability of the MWCNTs/MONPs nanocomposite following the next 500 cycles at 1100 mA g^{-1} is shown in **Figure 3**b. The specific discharge capacity slightly decreases from 595 mA h g^{-1} to 562 mA h g^{-1} in the initial seven cycles and then gradually increases to 680 mA h g^{-1} during the following 205 cycles. Such an uncommon trend of capacity rise upon cycling is well documented in literature and is mainly attributed to the reversible growth of a polymeric gel-like film resulting from kinetically activated electrolyte degradation.[37] The underneath mechanism of capacity rise along with cycling will also be investigated later in this work by electrochemical impedance spectroscope (EIS). During the last 288 cycles, the specific capacity slowly reduces to 537 mA h g^{-1}. In general, the ear-of-wheat-shaped nanocomposite holds a capacity retention of ~90% after 500 cycles at 1100 mA g^{-1}. The capacity loss is therefore only 0.02% per cycle, demonstrating the good cyclability of the biomimetic nanocomposite. Meanwhile, the coulombic efficiency climbs to ~99.5% after four cycles and keeps around to the end of the cycling.

Figure 3c presents the rate performance of the MWCNTs/MONPs nanocomposite at different current densities. The prototype cell was
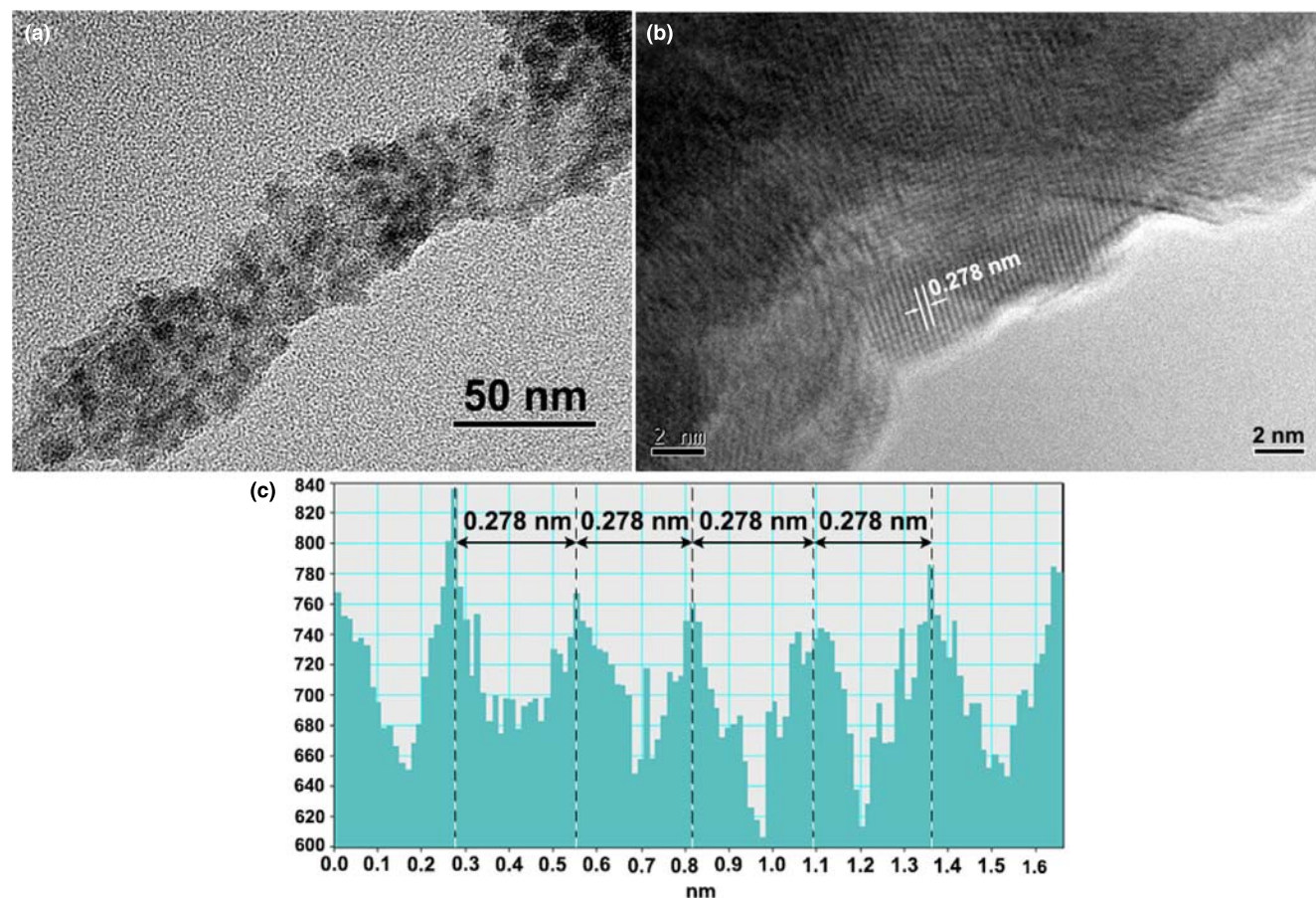
3

Figure 2. TEM image a), HRTEM image b), and interference fringe profiling c) of the biomimetic MWCNTs/MONPs nanocomposite.

first discharged/charged at 40 mA g^{-1} for five cycles. A reversible capacity of 800 mA h g^{-1} is delivered at the end of five cycles. It was then measured at 80, 320, 640, 1 280, and 2 560 mA g^{-1} for 50 cycles, respectively. The specific discharge capacity gradually increases from 632 to 811 mA h g^{-1} after 50 cycles at 80 mA g^{-1}. The capacity similarly rises from 668 to 787 mA h g^{-1} in the subsequent 50 cycles at 320 mA g^{-1} and is maintained at 709 mA h g^{-1} after another 50 cycles at 640 mA g^{-1}. When the current goes to 1 280 mA g^{-1}, the reversible capacity is roughly stabilized at 540 mA h g^{-1} during 50 cycles. At a higher current density of 2 560 mA g^{-1}, a specific capacity of 250 mA h g^{-1} is retained at the end of 50 cycles, which is even much higher than the theoretical capacity of Li$_4$Ti$_5$O$_{12}$.[8] Finally, the prototype battery was slowly cycled for five cycles with the current density that returned to 40 mA g^{-1} again. The capacity is about 880 mA h g^{-1} and almost 10% higher than what have been obtained before high current cycling, indicating that the fast cycling processes have little negative effect upon the electrochemical performance of the MWCNTs/MONPs nanocomposite. The coulombic efficiency maintains at around 99.5% during all measurements except for a break point on the switch of the current density. All these observations demonstrate the superior rate capability and cycling stability of the biomimetic MWCNTs/MONPs nanocomposite.

In order to further understand the mechanism of capacity rise upon cycling in **Figure 3**b,c, the electrochemical impedance spectra

of a prototype cell after different cycles were recorded. Shown in **Figure 4**a are the Nyquist plots of the cell at the fully charged state before cycling, after five cycles and after 105 cycles. All the spectra are composed of two depressed semicircles in the high and medium frequency regions and an inclined line in the low frequency region. **Figure 4**b shows the typical equivalent circuit of R$_s$(C$_{sei}$R$_{sei}$)(QR$_{ct}$)Z$_w$ for simulating the EIS, where, R$_s$ represents the resistance of Li$^+$ and electrons passing through the electrolyte and separator; C$_{sei}$ and R$_{sei}$ are the capacitance and resistance of the SEI layer, respectively; Q (CPE) and R$_{ct}$ are the charge transfer capacitance and resistance, respectively; Z$_w$ is the Warburg impedance associated with Li$^+$ diffusion.[38] One needs to note, an insertion capacitance C$_{int}$ corresponding to irreversible accumulation and consumption of Li$^+$ is required to fit the initial EIS. The simulated spectra profiles agree well with the measured ones as can be seen from the small chi-square. The simulation results are shown in **Table** 1. The R$_{sei}$ has little change during the first five cycles but is appreciably increased after 105 cycles, indicating the contribution of activated electrolyte on capacity rise upon cycling as also reported in literature.[32,39] Moreover, the R$_{ct}$ is noticeably reduced from 429.4 Ω cm^{-2} to 311.8 Ω cm^{-2} and 57.5 Ω cm^{-2} after five cycles and 105 cycles, respectively. The smaller charge transfer resistance possibly comes from the more beneficial interfaces in the battery along with cycling. As a consequence, the electric
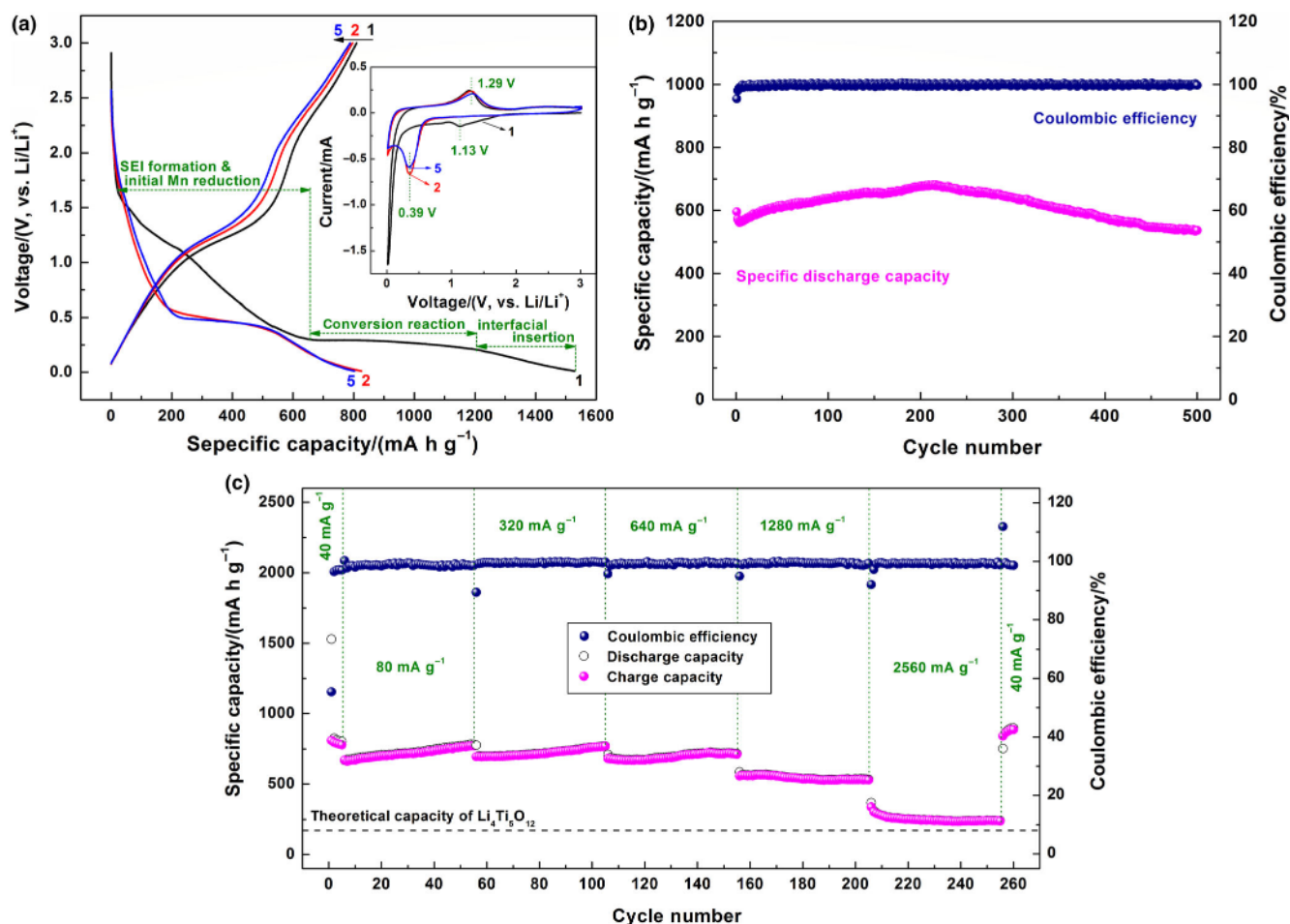
Figure 3. Galvanostatic discharge/charge profiles a), long-term cycling stability b), and rate capability at various current densities c) of the MWCNTs/MONPs nanocomposite. The current density in a) is 40 mA g^{-1} while its inset shows the CV curves at the scanning rate of 0.1 mV s^{-1}. The coulombic efficiency is shown as well in b) and c).
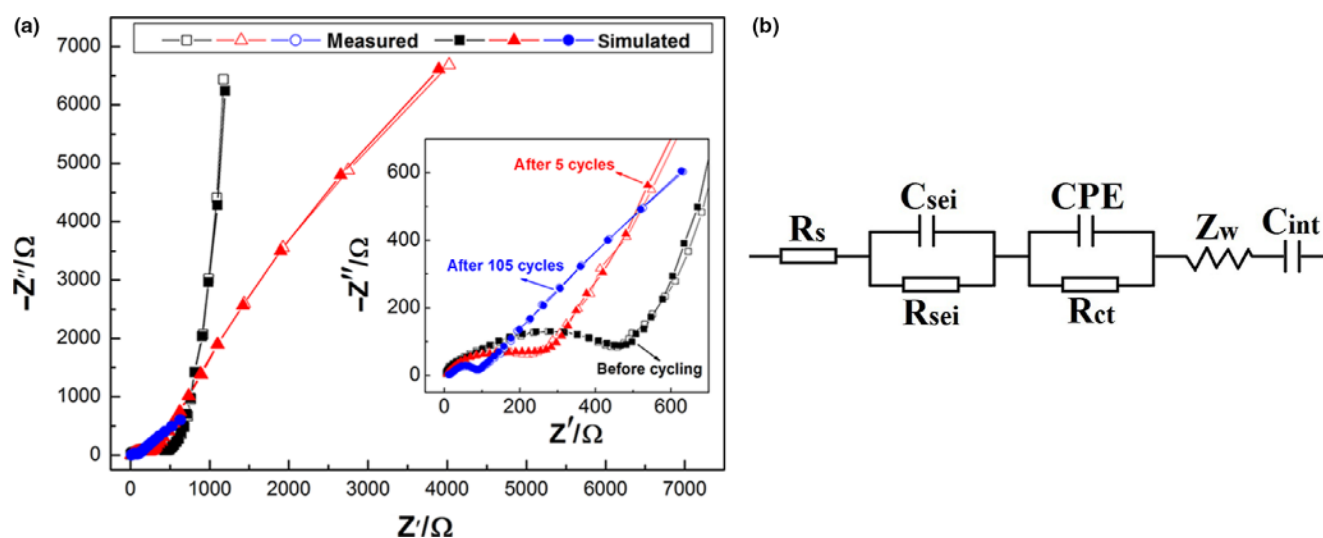

Figure 4. Electrochemical impedance spectra of the MWNCTs/MONPs composite electrode at the charged state after different cycles. a) The measured and simulated spectra and b) the equivalent electric circuit for simulation.

5

Table 1. Simulation results of the electrochemical impedance spectra from Figure 4.

	Before cycling	After 5 cycles	After 105 cycles
χ^2	3.626×10^{-3}	3.777×10^{-3}	2.257×10^{-3}
R_s (Ω cm^{-2})	2.716	2.745	6.14
C_{sei} (F cm^{-2})	8.529×10^{-7}	5.747×10^{-6}	1.812×10^{-5}
R_{sei} (Ω cm^{-2})	36.34	34.65	46.15
CPE, Yo (S s^n cm^{-2})	3.338×10^{-5}	0.000 96	0.005 292
n	0.6551	0.796 4	0.5423
R_{ct} (Ω cm^{-2})	429.4	311.8	57.5
Z_w (S s$^{0.5}$ cm^{-2})	0.003 688	0.001763	0.0002932
C_{int} (F cm^{-2})	0.003011	/	/

conductivity and cycling performance of the biomimetic MWCNTs/MONPs nanocomposite are prominently improved after an electrochemical activation process.

For comparison, the particle morphology and electrochemical performance of pure nanopowder Mn_3O_4 are investigated, and the results are shown in **Figure 5**. SEM image in **Figure 5**a indicates the particle size ranges from 20 to 40 nm, which is slightly larger than that of MONPs in the ear-of-wheat-shaped MWCNTs/MONPs nanocomposite. Therefore, MWCNTs are beneficial to control the particle size of Mn_3O_4 during solvothermal synthesis. **Figure 5**b displays the discharge/charge curves of pure nanopowder Mn_3O_4 at 50 mA g^{-1}. The initial discharge capacity is almost 1162 mA h g^{-1}, but the reversible charge capacity is only 576 mA h g^{-1} and quickly decreases to 505 mA h g^{-1} after five cycles. As shown in **Figure 5**c, the typical reversible capacity of pure nanopowder Mn_3O_4 at 100, 200, 400, 800, and 1600 mA g^{-1} is 430, 360, 295, 232, and 190 mA h g^{-1}, respectively. The cycling performances of the functionalized MWCNTs, pure nanopowder Mn_3O_4, and the MWCNTs/MONPs nanocomposite are compared in **Figure 5**d. The discharge/charge current is the same 160 mA g^{-1}, and the voltage range is the same 0.01–3.0 V. The specific discharge capacity of the functionalized MWCNTs stabilizes at about 175 mA h g^{-1} in 50 cycles with a coulombic efficiency higher than
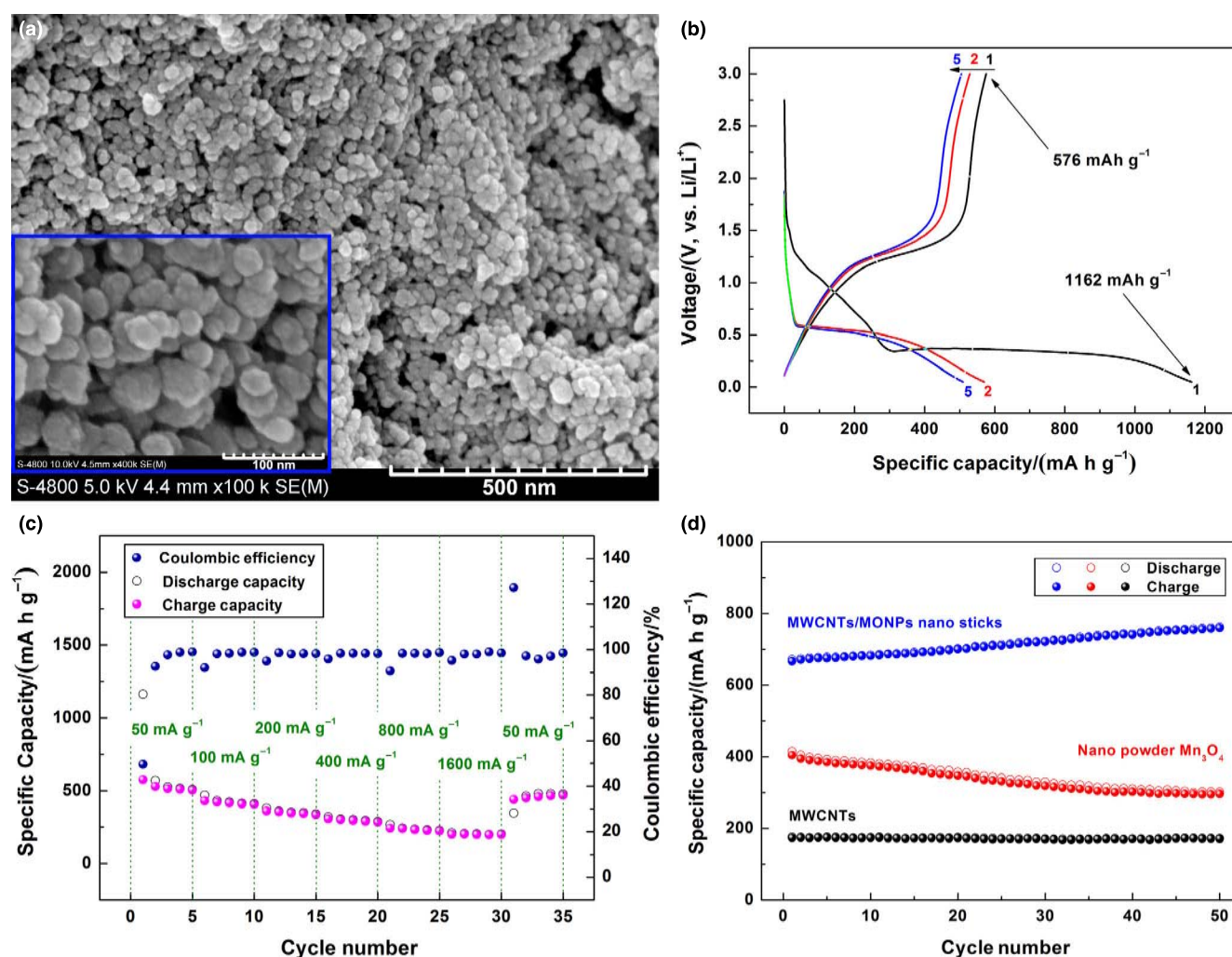

Figure 5. The SEM image a), discharge/charge curves b), rate c), and cycling d) performances of pure nanopowder Mn_3O_4. The measure current in b) is 50 mA g^{-1}. The cycling performances of the functionalized MWCNTs and that of the MWCNTs/MONPs nanocomposite are also shown in d) at the same current density of 160 mA g^{-1}.

Table 2. Performance comparison of the biomimetic MWCNTs/MONPs nanocomposite with recent literature.

Special Structure Reported	Current (mA g^{-1})	Cycles	Initial Capacity (mA h g^{-1})	Retained Capacity (mA h g^{-1})	Reference
Biomimetic ear-of-wheat-shaped MWCNTs/Mn$_3$O$_4$ nanocomposite	40	5	810	800	This Work
	160	50	645	796	
	320	50	668	787	
	1280	50	553	530	
Ultrathin-Mn$_3$O$_4$ nanosheets	200	300	340	520	[45]
Mn$_3$O$_4$ nanooctahedra	1000	56	314	239	[46]
Fluorine-doped Mn$_3$O$_4$ nanobelts	100	100	850	615	[47]
Fe-doped porous Mn$_3$O$_4$	200	100	850	615	[22]
	400	25	650	548	
	1200	25	476	453	
Mn$_3$O$_4$/carbon microspheres	500	100	~620	~490	[48]
Mn$_3$O$_4$/carbon nanofragments	0.1 C	100	627	566	[49]
Mn$_3$O$_4$/carbon yolk-shell nanorods	200	20	~590	381	[15]
Mn$_3$O$_4$/SWCNT macro-films	800	10	~460	~437	[29]
Mn$_3$O$_4$ nanorods/graphene	100	100	627	573	[50]
Graphene/Mn$_3$O$_4$ nanocomposite	100	100	802	702	[16]
3D arrays of Mn$_3$O$_4$ nanoblocks	292.5	5	~500	~490	[51]
Mn$_3$O$_4$ nanorods/Zn$_2$SnO$_4$ nanoneedles composite	100	50	817	577	[23]
	1000	50	550	441	
Fe$_3$O$_4$@C@Mn$_3$O$_4$ spheres	0.5 C	200	~500	358	[52]
Hierarchic CNTs@TiO$_2$@Mn$_3$O$_4$	500	40	489	333	[53]
PPy@Mn$_3$O$_4$/RGO composite	100	5	~560	~530	[54]
Mn$_3$O$_4$/CuO/TiO$_2$ submicroboxes	200	150	569	583	[55]

99%. However, the capacity of pure nanopowder Mn$_3$O$_4$ declines dramatically from 404 to 297 mA h g^{-1} after 50 cycles. Ultimately, not only a significantly large capacity the MWCNTs/MONPs nanocomposite delivers, but also a high-capacity retention upon cycling it maintains. The reversible specific capacity is visibly increased from 645 to 796 mA h g^{-1} in a similar trend as shown in **Figure 3**b,c. The capacity is almost twice of pure nanopowder Mn$_3$O$_4$ and is more than 4 times of the functionalized MWCNTs under the same experimental conditions. This could be attributed to the unique structure of the nanocomposite and the intimate interaction between the MWCNTs substrates and the surface ultrafine Mn$_3$O$_4$ nanoparticles as will be discussed below. In addition, the battery performance of this biomimetic MWCNTs/MONPs nanocomposite is compared with other Mn$_3$O$_4$-based electrode materials in recent literature. As one can see from **Table 2**, our ear-of-wheat-shaped MWCNTs/MONPs nanocomposite undoubtedly shows high reversible capacity, outstanding rate capability, and good cycling stability. Furthermore, the overall electrochemical performance is also superior comparing with other Mn-based oxides such as MnO/rGO,[40] CNT@MnO@N-doped carbon hetero-nanotubes,[41] Mn$_2$O$_3$@C,[42] MnO$_2$ nanorods/wires,[43] and MnO$_2$/aCNT.[44]

Figure 6 compares the SEM images of the MWCNTs/MONPs composite electrode before and after cycling with that of the pure nanopowder Mn$_3$O$_4$. The original electrode morphology before cycling is very similar as shown in **Figure 6**a,c. After 50 cycles at 100 mA g^{-1}, there are no obvious electrode crack and morphology change for MWCNTs/MONPs as seen in **Figure 6**b. On the contrary, serious electrode crack is observed in **Figure 6**d for cycled pure nanopowder Mn$_3$O$_4$ electrode, and even desquamation is found in the inset photograph. Hence, the good electrochemical performance of the MWCNTs/MONPs nanocomposite, including the high reversible capacity, superior rate capability, and good cycling stability, is ascribed to its special biomimetic nanostructure. For one thing, the MONPs directly grown on MWCNTs could greatly facilitate solid-state lithium transfer due to the large electrolyte/electrode contact area, abundant lithium accessible sites, short Li$^+$ diffusion path, and the good stability of the nanocomposite structure. For another, the MWCNTs in the nanocomposite could not only accommodate the strain induced by volume expansion/contraction of Mn$_3$O$_4$ during lithiation/delithiation, but also prevent the aggregation of Mn$_3$O$_4$ nanoparticles as well as the cracking of the electrode upon continuous cycling. Moreover, the MWCNTs could form a skeleton conducting network in the active material, efficiently improve the conductivity of the electrode, and remarkably stabilize the nanocomposite structure because of the intimate interaction between MWCNTs and the directly grown ultrafine Mn$_3$O$_4$ on their surface. As a result, both the lithium storage capability and electron transmission ability of transition metal oxides are noticeably improved due to the unique nanostructure of the novel biomimetic nanocomposite, leading
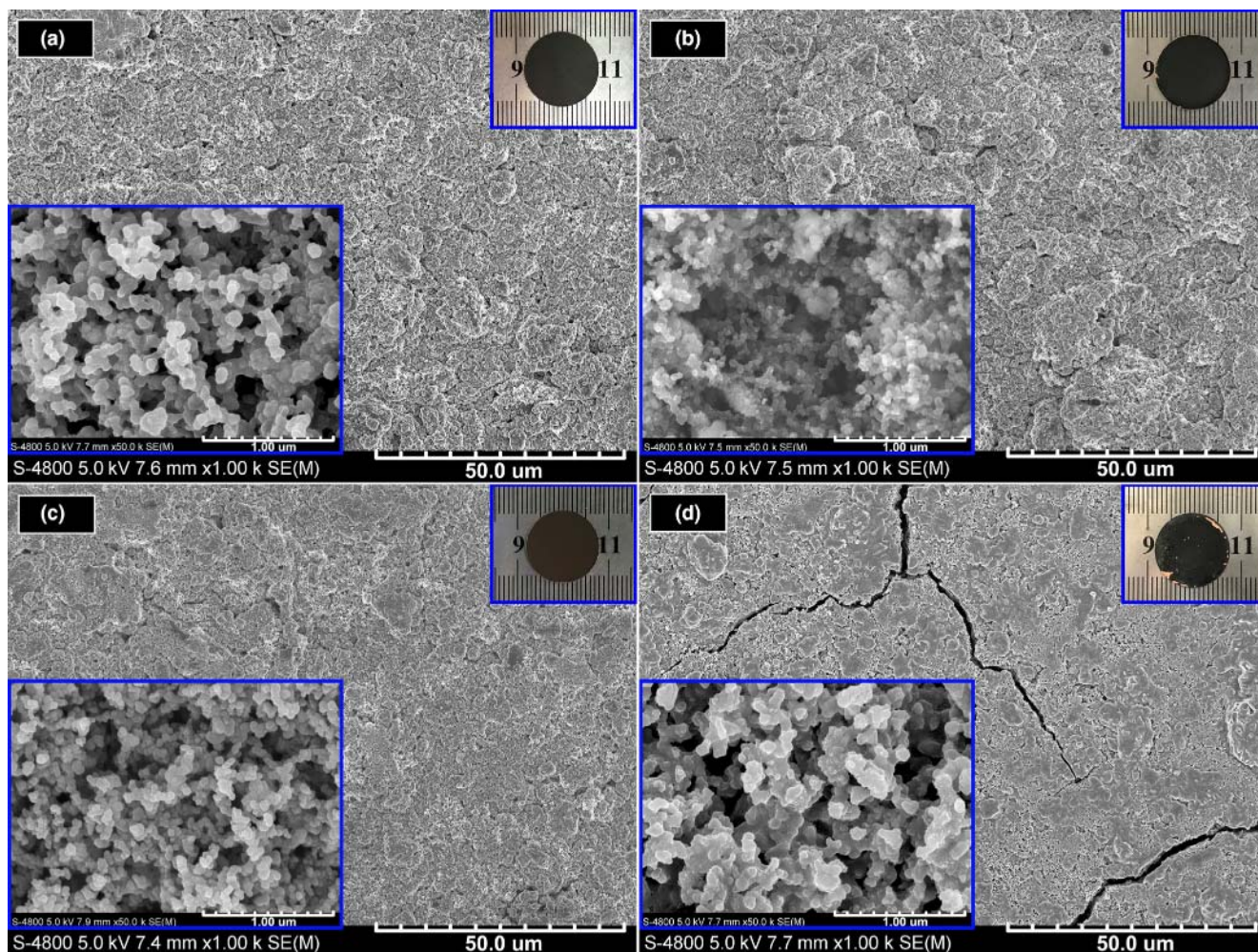
Figure 6. Comparison on the photograph pictures and SEM images of different electrodes. a) and b) are the as-prepared MWCNTs/MONPs nanocomposite electrode and that after 50 cycles at 100 mA g^{-1}, respectively. c) and d) are the pristine nanopowder Mn$_3$O$_4$ electrode and that after 50 cycles at 100 mA g^{-1}, respectively.

to favorable electrochemical performance for rechargeable lithium batteries.

3. Conclusion

In this study, we report a facile solvothermal method to synthesize the ear-of-wheat-shaped MWCNTs/MONPs nanocomposite anode material for lithium-ion batteries. Thanks to the unique nanostructure of ultra-fine Mn$_3$O$_4$ particles tightly grown on functionalized MWCNT skeletons, the novel biomimetic composite material possesses favorable lithium storage ability and electric conductivity simultaneously, and thus shows high and reversible capacities along with cycling at various current rates. This simple synthetic method can be potentially applied to the design and preparation of other energy materials for lithium/sodium batteries and fuel cells. Further fundamental work is also needed to identify the synergetic lithiation/delithiation process of each component (MONPs and MWCNTs, respectively) during electrochemical discharging/charging.

4. Experimental Section

The as-received MWCNTs were first functionalized by sonication in a concentration mixture of H$_2$SO$_4$ and HNO$_3$ as introduced in detail elsewhere.[25,26] A total of 0.192 g so-functionalized MWCNTs was dissolved in 40 mL ethanol followed with 2 h sonication. A total of 0.632 g KMnO$_4$ was then added under vigorous stirring for 1 h at room temperature. The mixed solution was transferred into a Teflon-lined stainless steel autoclave and sealed into an oven at 180 °C for 12 h. After natural cooling down to ambient temperature, the black products were collected, rinsed, and then dried at 80 °C for 24 h under vacuum. For comparison, pure Mn$_3$O$_4$ nanopowders were also synthesized via a similar procedure but without adding MWCNTs.

Powder X-ray diffraction (XRD) pattern was taken on a Bruker D8 Advance X-ray diffractometer using filtered Cu Kα radiation (λ = 1.540 6 Å), and Rietveld refinement was performed to acquire the crystallographic parameters. Particle size, morphology, and microstructures of the nanomaterials were studied using scanning electron microscope (SEM, Hitachi S-4800) and transmission electron

microscope (TEM, JEM 2100). A thin layer of platinum (Pt) was spin-coated on the specimens before SEM observation to prevent from charge accumulation. Element distribution was analyzed by recording the energy-dispersive X-ray spectrum (EDX) simultaneously with SEM observation. The cycled battery electrode was disassembled in an argon-filled glove box and rinsed with dimethyl carbonate (DMC) for several times before SEM imaging.

The electrochemical measurements were implemented using CR2016 coin cells assembled in the glove box where water and oxygen were both controlled <0.1 ppm. The working electrodes were fabricated by mixing the active material, carbon black, and polyvinylidene fluorine (PVDF) in a weight ratio of 80:10:10 in N-methyl-2-pyrrolidone (NMP). The resultant slurry was uniformly pasted onto copper foil and dried at 120 °C overnight in vacuum. A total of 1.0 mol L^{-1} $LiPF_6$ in ethylene carbonate (EC) and dimethyl carbonate (DMC) (1:1, volume ratio) was employed as the electrolyte. Pure lithium foil was used as the counter electrode. The prototype batteries were discharged/charged at constant currents by a CT2001A LAND Battery Testing System to evaluate the battery performance in the galvanostatic mode at room temperature. The cyclic voltammetry (CV) was performed on a Versatile Multichannel Potentiostat 2/Z (VMP2, Princeton Applied Research) between 0.01 and 3.0 V at the scanning rate of 0.1 mV s^{-1}. The electrochemical impedance spectroscopy (EIS) was carried out also on the VMP2 by applying a 5 mV amplitude signal in the frequency range from 1 mHz to 100 kHz. The EIS spectra were simulated by the ZSimpWin package.

Acknowledgements

Conflict of Interest

The authors declare no conflict of interest.

Keywords

References

[1] M. Armand, J. M. Tarascon, *Nature* **2008**, *451*, 652.
[2] J. W. Choi, D. Aurbach, *Nat. Rev. Mater.* **2016**, *1*, 16013.
[3] Y. Y. Liu, Y. Y. Zhu, Y. Cui, *Nat. Energy* **2019**, *4*, 540.
[4] D. Larcher, J. M. Tarascon, *Nat. Chem.* **2015**, *7*, 19.
[5] H. J. Xu, Y. R. Yu, Z. Wang, G. S. Shao, *Energy Environ. Mater.* **2019**, *2*, 234
[6] Y. P. Wu, E. Rahm, R. Holze, *J. Power Sources* **2003**, *114*, 228.
[7] M. V. Reddy, G. V. Subba Rao, B. V. R. Chowdari, *Chem. Rev.* **2013**, *113*, 5364.
[8] S. W. Wang, Q. Liu, C. L. Zhao, F. Z. Lv, X. Y. Qin, H. D. Du, F. Y. Kang, B. H. Li, *Energy Environ. Mater.* **2018**, *1*, 28.
[9] M. T. F. Rodrigues, G. Babu, H. Gullapalli, K. Kalaga, F. N. Sayed, K. Kato, J. Joyner, P. M. Ajayan, *Nat. Energy* **2017**, *2*, 17108.
[10] Z. Yi, Z. M. Wang, Y. Cheng, L. M. Wang, *Energy Environ. Mater.* **2018**, *1*, 132.
[11] K. J. Griffith, K. M. Wiaderek, G. Cibin, L. E. Marbella, C. P. Grey, *Nature* **2018**, *559*, 556.
[12] L. Wu, J. Zheng, L. Wang, X. Xiong, Y. Shao, G. Wang, J.-H. Wang, S. Zhong, M. Wu, *Angew. Chem. Int. Ed.* **2019**, *58*, 811.
[13] P. Poizot, S. Laruelle, S. Grugeon, L. Dupont, J. M. Tarascon, *Nature* **2000**, *407*, 496.
[14] Y. Ma, *Energy Environ. Mater.* **2018**, *1*, 148.
[15] Z. Y. Cai, L. Xu, M. Y. Yan, C. H. Han, L. He, K. M. Hercule, C. J. Niu, Z. F. Yuan, W. W. Xu, L. B. Qu, K. N. Zhao, L. Q. Mai, *Nano Lett.* **2015**, *15*, 738.
[16] J. G. Wang, D. D. Jin, R. Zhou, X. Li, X. R. Liu, C. Shen, K. Y. Xie, B. H. Li, F. Y. Kang, B. Q. Wei, *ACS Nano* **2016**, *10*, 6227.
[17] J. Mei, T. Liao, L. Z. Kou, Z. Q. Sun, *Adv. Mater.* **2017**, *29*, 1700176.
[18] J. Jiang, Y. Y. Li, J. P. Liu, X. T. Huang, C. Z. Yuan, X. W. Lou, *Adv. Mater.* **2012**, *24*, 5166.
[19] Y. M. Sun, N. A. Liu, Y. Cui, *Nat. Energy* **2016**, *1*, 16071.
[20] J. Lu, Z. H. Chen, Z. F. Ma, F. Pan, L. A. Curtiss, K. Amine, *Nat. Nanotechnol.* **2016**, *11*, 1031.
[21] J. Su, H. W. Song, C. X. Wang, *Adv. Funct. Mater.* **2019**, 1907154.
[22] Y. Ma, C. L. Fang, B. Ding, G. Ji, J. Y. Lee, *Adv. Mater.* **2013**, *25*, 4646.
[23] R. R. Zhang, Y. Y. He, A. H. Li, L. Q. Xu, *Nanoscale* **2014**, *6*, 14221.
[24] R. Zhang, D. Wang, L. C. Qin, G. W. Wen, H. Pan, Y. F. Zhang, N. Tian, Y. Zhou, X. X. Huang, *J. Mater. Chem. A* **2017**, *5*, 17001.
[25] X. F. Sun, Y. L. Xu, J. Wang, *J. Solid State Electrochem.* **2012**, *16*, 1781.
[26] X. F. Sun, Y. L. Xu, P. Ding, G. G. Chen, X. Y. Zheng, R. Zhang, L. Li, *J. Power Sources* **2014**, *255*, 163.
[27] X. F. Sun, Y. L. Xu, P. Ding, M. R. Jia, G. Ceder, *J. Power Sources* **2013**, *244*, 690.
[28] I. Djerdj, D. Arcon, Z. Jaglicic, M. Niederberger, *J. Phys. Chem. C* **2007**, *111*, 3614.
[29] J. W. Qin, Q. Zhang, Z. Y. Cao, X. Li, C. W. Hu, B. Q. Wei, *Nano Energy* **2013**, *2*, 733.
[30] H. Li, P. Balaya, J. Maier, *J. Electrochem. Soc.* **2004**, *151*, A1878.
[31] O. Delmer, P. Balaya, L. Kienle, J. Maier, *Adv. Mater.* **2008**, *20*, 501.
[32] S. Zhu, J. J. Li, X. Y. Deng, C. N. He, E. Z. Liu, F. He, C. S. Shi, N. Q. Zhao, *Adv. Funct. Mater.* **2017**, *27*, 1605017.
[33] S. H. Wu, G. L. Fu, W. Q. Lv, J. K. Wei, W. J. Chen, H. Q. Yi, M. Gu, X. D. Bai, L. Zhu, C. Tan, Y. C. Liang, G. L. Zhu, J. R. He, X. Q. Wang, K. H. L. Zhang, J. Xiong, W. D. He, *Small* **2017**, *14*, 1702667.
[34] G. M. Li, Y. Li, J. Chen, P. P. Zhao, D. G. Li, Y. H. Dong, L. P. Zhang, *Electrochim. Acta* **2017**, *245*, 941.
[35] X. F. Meng, Y. L. Xu, X. F. Sun, J. Wang, L. L. Xiong, X. F. Du, S. C. Mao, *J. Mater. Chem. A* **2015**, *3*, 12938.
[36] K. F. Zhong, B. Zhang, S. H. Luo, W. Wen, H. Li, X. J. Huang, L. Q. Chen, *J. Power Sources* **2011**, *196*, 6802.
[37] J. Z. Wang, N. Du, H. Wu, H. Zhang, J. X. Yu, D. R. Yang, *J. Power Sources* **2013**, *222*, 32.
[38] X. F. Sun, Y. L. Xu, M. R. Jia, P. Ding, Y. H. Liu, K. Chen, *J. Mater. Chem. A* **2013**, *1*, 2501.
[39] J. Tang, W. Liu, H. L. Wang, A. Gomez, *Adv. Mater.* **2016**, *28*, 10298.
[40] H. Raj, A. Sil, N. V. Pulagara, *Ceram. Int.* **2019**, *45*, 14829.
[41] Y. Wang, H. Wu, Z. Liu, H. Zhao, L. Huang, Q. Wang, H. Liu, Y. Zhang, *Electrochim. Acta* **2019**, *304*, 158.

[42] S. Li, B. Li, Y. Zhong, Z. Pan, M. Xu, Y. Qiu, Q. Huang, W. Li, *Mater. Chem. Phys.* **2019**, *222*, 256.

[43] N. Palaniyandy, F. P. Nkosi, K. Raju, K. I. Ozoemena, *J. Electroanal. Chem.* **2019**, *833*, 79.

[44] D. Wang, K. Wang, L. Sun, H. Wu, J. Wang, Y. Zhao, L. Yan, Y. Luo, K. Jiang, Q. Li, S. Fan, J. Li, J. Wang, *Carbon* **2018**, *139*, 145.

[45] M. M. Zhen, Z. Zhang, Q. T. Ren, L. Liu, *Mater. Lett.* **2016**, *177*, 21.

[46] Q. Hao, J. P. Wang, C. X. Xu, *J. Mater. Chem. A* **2014**, *2*, 87.

[47] R. C. Jin, H. Liu, Y. S. Guan, J. H. Zhou, G. H. Li, *CrystEngComm* **2015**, *17*, 7717.

[48] Y. N. Ko, S. Bin Park, S. H. Choi, Y. C. Kang, *Sci. Rep.* **2014**, *4*, 5751.

[49] Y. C. Zhuang, Z. Ma, Y. M. Deng, X. N. Song, X. X. Zuo, X. Xiao, J. M. Nan, *Electrochim. Acta* **2017**, *245*, 440.

[50] S. K. Park, C. Y. Seong, S. Yoo, Y. Piao, *Energy* **2016**, *99*, 266.

[51] Y. Nakagawa, H. Kageyama, R. Matsumoto, Y. Oaki, H. Imai, *Nanoscale* **2015**, *7*, 18471.

[52] Y. Zhang, K. Q. Yue, H. S. Zhao, Y. Wu, L. F. Duan, K. L. Wang, *Chem. Eng. J.* **2016**, *291*, 238.

[53] D. J. Yan, X. D. Zhu, Y. C. Mao, S. Y. Qiu, L. L. Gu, Y. J. Feng, K. N. Sun, *J. Mater. Chem. A* **2017**, *5*, 17048.

[54] Y. R. Ren, J. W. Wang, X. B. Huang, J. N. Ding, *Electrochim. Acta* **2015**, *186*, 345.

[55] P. Liu, X. F. Xia, W. Lei, Q. L. Hao, *Chem. Eng. J.* **2017**, *316*, 214.